

# The Properties of Poor Groups of Galaxies: II. X-ray and Optical Comparisons

John S. Mulchaey<sup>1</sup> and Ann I. Zabludoff<sup>1,2</sup>

## ABSTRACT

We use ROSAT PSPC data to study the X-ray properties of a sample of twelve poor groups that have extensive membership information (Zabludoff & Mulchaey 1997; Paper I). Diffuse X-ray emission is detected in nine of these groups. In all but one of the X-ray detected groups, the X-ray emission is centered on a luminous elliptical galaxy. Fits to the surface brightness profiles of the X-ray emission suggest the presence of *two* X-ray components in these groups. The first component is centered on the central elliptical galaxy and is extended on scales of 20–40  $h_{100}^{-1}$  kpc. The location and extent of this component, combined with its X-ray temperature ( $\sim 0.7\text{--}0.9$  keV) and luminosity ( $\sim 10^{41\text{--}42} h_{100}^{-2}$  erg s<sup>-1</sup>), favor an origin in the interstellar medium of the central galaxy. Alternatively, the central component may be the result of a large-scale cooling flow.

The second X-ray component is detected out to a radius of at least  $\sim 100\text{--}300 h_{100}^{-1}$  kpc. This component follows the same relationships found among the X-ray temperature (T), X-ray luminosity ( $L_X$ ) and optical velocity dispersion ( $\sigma_r$ ) of rich clusters. This result suggests that the X-ray detected groups are low-mass versions of clusters and that the extended gas component can properly be called the intragroup medium, in analogy to the intracluster medium in clusters. The failure to detect an intragroup medium in the three groups with very low velocity dispersions is consistent with their predicted X-ray luminosities and temperatures based on the relationships derived for clusters and X-ray detected groups. The best-fit value of  $\beta$  derived from the  $\sigma_r$ -T relationship for groups and clusters is  $\sim 0.99 \pm 0.08$ , implying that the galaxies and hot gas trace the same potential with equal energy per unit mass and that the groups are dynamically relaxed.

---

<sup>1</sup>Observatories of the Carnegie Institution of Washington, 813 Santa Barbara St., Pasadena, CA 91101, E-mail: mulchaey@pegasus.ociw.edu

<sup>2</sup>UCO/Lick Observatory and Board of Astronomy and Astrophysics, University of California at Santa Cruz, Santa Cruz, CA, 95064, E-mail: aiz@ucolick.org

We also find a trend for the position angle of the optical light in the central elliptical galaxy to align with the position angle of the large-scale X-ray emission. This trend is consistent with that found for some rich clusters containing cD galaxies (Rhee, van Haarlem & Katgert 1992; Sarazin et al. 1995; Allen et al. 1995). The alignment of the central galaxy with the extended X-ray emission suggests that the formation and/or evolution of the central galaxy is linked to the shape of the global group potential. One possible scenario is that the central galaxy formed via galaxy-galaxy mergers early in the lifetime of the group and has not been subject to significant dynamical evolution recently.

*Subject headings:* galaxies: compact–galaxies: intergalactic medium–cosmology: dark matter–X-rays: galaxies

## 1. Introduction

Because most galaxies occur in small groups, understanding the physical nature of these systems is critical for cosmology. An outstanding question is whether poor groups are simply low-mass versions of richer clusters or physically different systems. Establishing the nature of groups has proved difficult because these systems typically contain only three or four bright galaxies. Thus, it is not even known if the majority of the cataloged groups are real, bound systems or if they are simply chance superpositions (e.g., Ramella et al. 1989; Hernquist et al. 1995).

The presence of diffuse X-ray emission provides evidence for a common potential in some poor groups (e.g., Mulchaey et al. 1993, Ponman & Bertram 1993, David et al. 1994, Ebeling et al. 1995, Pildis et al. 1995, Henry et al. 1995, Mulchaey et al. 1996a, Ponman et al. 1996, Burns et al. 1996). Many ROSAT studies suggest there is a correlation between the morphological composition of the group and the existence of X-ray emission (e.g., Ebeling et al. 1995, Pildis et al. 1995, Henry et al. 1995, Mulchaey et al. 1996a), providing further evidence for the reality of the X-ray detected groups. However, it is still possible that the X-ray gas is merely a projection of unbound gas in filaments along the line-of-sight (Hernquist et al. 1995).

Perhaps the best way to establish the physical reality of groups is to extend the kinematic properties of these systems to include much fainter members. We have recently completed a fiber spectroscopy study of a sample of twelve poor groups (Zabludoff &

Mulchaey 1997; Paper I) and have shown that the X-ray detected groups are indeed bound systems. Even if the reality of some groups has been demonstrated, there is still controversy about the origin of the X-ray emission in these systems. For example, both Dell’Antonio et al. (1994) and Mahdavi et al. (1997) find a much flatter relationship between X-ray luminosity and velocity dispersion ( $\sigma_r$ ) for groups than is found for rich clusters. These authors argue that the X-ray emission in groups is dominated by emission from individual galaxies and not from a global group potential. In contrast, Ponman et al. (1996) remove the X-ray emission from individual galaxies and find reasonable agreement between the  $L_X$ – $\sigma_r$  relationship for Hickson Compact Groups (HCGs) and rich clusters. Henry et al. (1995) and Burns et al. (1996) also find that the X-ray luminosity function is a natural extension of the relationship for clusters, implying a similar physical mechanism for the X-ray emission. However, both the Henry et al. (1995) and Burns et al. (1996) studies only include the most X-ray luminous groups and not the more typical, low luminosity systems where the differences in the  $L_X$ – $\sigma_r$  relationship have been reported.

Some of the uncertainty in the  $L_X$ – $\sigma_r$  relationship and in other comparisons of optical and X-ray properties may result from poorly determined optical properties. For most groups, velocity dispersions have been estimated from as few as three or four galaxy velocity measurements. However, in Paper I we showed that calculating  $\sigma_r$  from only a few galaxies can result in large uncertainties in the measurement, often underestimating  $\sigma_r$  by a factor of 1.5 or more. Thus, the values of  $\sigma_r$  used in many previous comparisons of the optical and X-ray properties of groups may be flawed.

The X-ray observations of poor groups are also subject to large uncertainties that in general do not plague similar measurements in rich clusters. For example, diffuse emission from the global potential dominates the cluster X-ray emission. However, in poor groups, the contribution of X-rays from individual galaxies may be substantial. The presence of luminous X-ray emission in poor groups is found predominantly in systems with a central elliptical galaxy (e.g., Mulchaey et al. 1996a). The expected X-ray emission from such a galaxy can be comparable to the diffuse, extended emission observed in many groups. Thus, it is not clear whether the observed emission is associated with an extended halo of the central galaxy (e.g., Trinchieri et al. 1997) or represents hot gas in the group’s global potential. If the observed emission is dominated by a component from the central galaxy’s interstellar medium, comparisons with global group properties such as velocity dispersion may not be particularly meaningful.

In Paper I, we showed that X-ray detected groups typically contain at least  $\sim 20$ -50 members to absolute magnitudes of  $M_B \sim -14$  to  $-16 + 5 \log_{10} h_{100}$ . With this many galaxy velocities available, we are able to calculate robust velocity dispersions for poor groups.

Here we use deep ROSAT observations of the twelve groups studied in Paper I to examine the nature of the X-ray emission in these systems. In the next section, we describe the ROSAT observations and data reduction techniques. In §3, we study the spatial distribution of the X-ray emission and discuss the evidence for two X-ray components in these groups. Spectral analysis of the ROSAT data, including temperature and luminosity measurements, are presented in §4. Comparisons of the derived optical and X-ray properties of groups are given in §5, and our conclusions are summarized in §6. All distance-dependent quantities in this paper are calculated assuming  $H_0 = 100 \text{ km s}^{-1} \text{ Mpc}^{-1}$  ( $h=H_0/100$ ).

## 2. ROSAT Observations and Data Reduction

ROSAT PSPC observations were extracted from the archive for the group sample given in Table 1. In all cases, the PSPC observation is centered on the group. To search for diffuse gas in these systems, we followed the reduction method outlined in Mulchaey et al. (1996a). Times of high background are identified and excluded by discarding any data taken when the Master Veto rate is greater than  $170 \text{ counts s}^{-1}$ . The final exposure time used in each case is given in Table 1. For each group four images are created corresponding to the energy bands above 0.5 keV described in Snowden et al. (1994). These images are corrected for vignetting using energy-dependent exposure maps. The four images are then co-added to produce a 0.5–2 keV image.

Before the X-ray emission from the group can be studied, emission from *unrelated* sources must be removed. We find these sources using the task “DETECT” in the Extended Object and X-ray Background Analysis software (Snowden 1994), which identifies ‘point sources’ in the field. In the context of this discussion, ‘point source’ refers to a source that appears point-like at the resolution of the ROSAT PSPC ( $\text{FWHM} \sim 30''$  corresponding to  $\sim 10 h^{-1} \text{ kpc}$  for our most distant group; the resolution is considerably worse for sources far off-axis). Emission from point sources is then removed by excluding a circular region around each source with a radius 1.5 times the radius that encircles 90% of the source flux. This exclusion radius corresponds to  $1.5'$  for sources on-axis (Hasinger et al. 1992). To verify that the majority of these point sources are truly unrelated to the group, we compare the positions of the identified point sources with the positions of the known group members identified in Paper I. For most (9 of 12) of the groups, only one or two of the group members are X-ray sources. The group with the most associated sources is HCG 90, where four of the galaxies are X-ray emitters. However, two of these galaxies are Seyferts, so the X-ray emission is probably not related to the gravitational potential of the group or

the interstellar medium of the host galaxies. Even in this extreme case, more than 90% of the point sources identified appear to be unrelated to the group. Given the high rate of ‘contaminating’ sources in these fields, we exclude all point sources found by “DETECT” (except the central galaxy emission; see below).

The resulting (unsmoothed) image is then examined for evidence of diffuse emission. In 9 of the 12 fields, a diffuse component is clearly visible. To our knowledge, the diffuse emission detection in the NGC 4325 group has not previously been reported. All the other positive detections are documented in the literature (NGC 533, NGC 5129 and NGC 5846: Mulchaey et al. 1996a, NGC 741: Doe et al. 1995, NGC 2563: Trinchieri, Fabbiano & Kim 1997; HCG 42 and HCG 90: Ponman et al. 1996, HCG 62: Ponman & Bertram 1993, Pildis et al. 1995). Diffuse emission is also found  $\sim 14'$  north of the NGC 7582 group center. However, this emission is coincident with the background cluster Abell S1111 and thus almost certainly originates in the rich cluster, so we count this system among our non-X-ray detected groups. In the NGC 491 and NGC 664 fields, no diffuse emission is detected.

### 3. Spatial Analysis of the Diffuse Gas

In Figure 1, we overlay the contours for the diffuse X-ray emission on the STScI Digitized Sky Survey images of the group fields. With the exception of HCG 90, the X-ray emission is always peaked within  $5\text{--}10\text{ h}^{-1}\text{ kpc}$  of a giant elliptical galaxy, which is the brightest group galaxy (BGG). In Paper I, we showed that the BGG lies near the kinematic and projected spatial center of the group, suggesting it is coincident with the core of the group potential (see §3.4 of Paper I). For this reason, it may be proper to include the X-ray emission at the location of the BGG as part of the intragroup gas and we have included this emission in Figure 1 (except for HCG 90). All other emission due to point sources in the field has been removed.

For the groups with a detected diffuse component, an azimuthally-averaged surface brightness profile is constructed. The inner bin in each profile corresponds to a physical radius of  $\sim 3\text{ h}^{-1}\text{ kpc}$ . We model the surface brightness profiles using a modified King function:

$$S(R) = S_o (1.0 + (R/R_{\text{core}})^2)^{-3\beta+0.5}$$

with a constant background included in the fit. The models are convolved with the 1 keV PSPC point spread function, and then fit to the data with  $S_o$ ,  $R_{\text{core}}$ ,  $\beta$  and the constant background as free parameters. For all but one of the groups with a BGG, the fits with a

single model are unacceptable (i.e., reduced chi-squared values  $> 2.0$ ). In general, there is a shoulder in the profile at  $\sim 2\text{-}3'$ , which suggests the presence of two X-ray components.

To test for the presence of two components, we fit the surface brightness profiles with two King models. Our fitting method is as follows. First, we fit the surface brightness profile beyond  $5'$  with a single King model and a constant for the background. A single King model provides a good fit to the extended component (see Table 2). Next, we fit the entire profile with the two component model, fixing the shape (i.e.,  $\beta$  and  $R_{\text{core}}$ ) of the extended component to the values found in the fit beyond  $5'$ . To verify that this fitting method produces robust results, we varied the inner radius over which the extended component was originally fit from  $3'$  up to  $10'$ . While the best fit parameters for the extended component were found to vary somewhat with the choice of the inner radius, they are consistent within the errors with those determined in the initial fits (i.e., using an inner radius of  $5'$ ). Thus, although an inner radius of  $5'$  corresponds to a different physical scale for each group, we do not believe this choice strongly effects our final fit results. The parameters of the core component in the two King model fits are relatively insensitive to the adopted model for the extended gas.

In general, the two component models provide a very good fit to the data and a significant improvement over the single King model (Figure 2 and Table 2). The success of this model argues for the presence of two X-ray components in each of these groups. One possibility is that the X-ray emission from the core component originates in the interstellar medium of the central galaxy (the BGG), while the extended component corresponds to gas in the global group potential (i.e., an intragroup medium). Ibeke et al. (1996) have suggested a similar model for the poor cluster Fornax, attributing the sharp upturn in the surface brightness profile at small radii to emission from the central galaxy and the extended component to emission from the intracluster medium. The X-ray properties of the two components in poor groups appear to be consistent with a similar interpretation. We examine this idea further in §5.

An interesting consequence of the two component models is that the derived slopes of the King profiles (i.e.,  $\beta$ ) for both components tend to be much steeper than is implied from a single King model fit to the observed emission. Mathematically this behavior is expected when a narrow/brighter beta model and a wider/fainter beta model are added together (Makishima 1995). The larger values of  $\beta$  implied from the two component fits has several important implications for groups. In a model where both the gas and galaxies are isothermal and in equilibrium,  $\beta$  is simply the square of the ratio of the galaxy to gas velocity dispersion:

$$\beta = \sigma_r^2 \mu m_p / kT$$

where  $\mu$  is the mean molecular weight in amu,  $m_p$  is the mass of the proton,  $\sigma_r$  is the one-dimensional velocity dispersion and  $T$  is the temperature of the gas. Previous X-ray studies of groups suggested low values of  $\beta$  for the extended gas, implying that the energy per unit mass is higher in the gas than in the galaxies. However, our two component fits are consistent within the errors with  $\beta \sim 1$  for the extended component in many cases. Thus, significant heating of the gas by non-gravitational processes may not be required in these groups. Furthermore, many of the derived physical parameters for groups such as the total group mass and the fraction of mass in hot gas depend on the value of  $\beta$  assumed. For example, for a fixed X-ray luminosity, higher values of  $\beta$  lead to significantly lower gas masses. Thus, if our  $\beta$  values are correct, the baryonic mass in hot gas may be less than what has been inferred in some previous studies. The  $\beta$  parameter can also be derived independently from direct measurements of  $\sigma_r$  and of temperature as we discuss in §5.

While the evidence for two X-ray components in these poor groups is compelling, the parameters derived from the King model fits depend strongly on the assumptions made. In general, most of the derived X-ray properties of groups are poorly determined compared with rich clusters, which have a higher surface brightness and a lower level of relative contamination from individual galaxies. Still, many of the effects that we find may also be relevant to the X-ray properties of richer systems. For example, in analogy to the X-ray detected groups, we might expect a second X-ray component to be associated with the central galaxy in cD-dominated clusters. Although this component might be more difficult to discern against the more luminous intracluster medium, it would probably have a non-negligible effect on the surface brightness profile and derived physical quantities like  $\beta$ .

#### 4. Spectral Analysis

Given the results of the surface brightness profiles, we have extracted three spectra for most of the X-ray detected groups: i) one for the central component, ii) one for the extended gas component, and iii) one with both the extended and central components included. Because it is not possible to spectroscopically isolate the central emission from the extended emission with the ROSAT PSPC data, we assume that the flux in the inner  $1.5'$  is dominated by the central emission and that the rest of the flux is from the extended component. The only exception is the closest of the X-ray detected groups NGC 5846, where we assume that all the flux within  $3'$  of the center is from the central component (see Figure 2). For the NGC 5129 group there are insufficient counts in the central component

to study it spectroscopically, so we have extracted a spectrum for the extended gas only. In the case of HCG 90, where the diffuse gas is not centered on a particular galaxy, we also extract only a diffuse spectrum.

The maximum extent of each spectral extraction is given in column 3 of Table 3. For five of the nine groups with an extended component, the maximum extraction radius corresponds to  $0.3 \text{ h}^{-1} \text{ Mpc}$ . This radius is chosen because it is the smallest radius within which there are enough galaxy velocity measurements so that we can obtain a reliable velocity dispersion for the groups (see Paper I). However, for HCG 42, NGC 5846 and HCG 90, the diffuse X-ray emission is detected to only a fraction of  $0.3 \text{ h}^{-1} \text{ Mpc}$ . The spectra for these three groups were extracted at a radius where the surface brightness of the diffuse gas reaches 20% of the determined background level. Point sources were excluded from each spectral extraction using the circular regions described in §2. The background region in each case was an annulus with an inner radius beyond the edge of the detectable emission. Each spectrum was fit with two different spectral models. The first model was a Raymond-Smith plasma model with variable abundances and fixed absorbing column. The results of these fits are given in columns 4–6 of Table 3 (all quoted errors are for the 90% confidence level). In general, good fits to the data are found with this model (i.e., reduced chi-squared less than 1.5). Good fits are also obtained with a MEKA plasma model (Mewe, Gronenschild & van den Oord 1985) and variable abundances (see columns 7–9 of Table 3). An examination of the temperatures and abundances derived from the two spectral models reveals good agreement between the models for the systems studied here. While the metal abundances implied tend to be very low, we caution the reader that this quantity may not be reliably determined with the ROSAT PSPC (cf. Bauer & Bregman 1996) and so strong statements about the gas enrichment cannot be made with the current dataset. To determine the effects of the metallicities on the derived gas temperatures, we also fit the diffuse spectrum of each group with a Raymond-Smith model with the metallicity fixed at half solar (Table 3). With this assumed metallicity, the derived gas temperatures were typically  $\sim 10\%$  higher, consistent within the errors to the best-fit value in the model where the abundance was allowed to vary.

For three of the groups, the diffuse gas spectrum has enough counts that a rough temperature profile can be determined. In these cases, we have extracted spectra in several annuli, which were chosen to contain  $\sim 1000$  counts in each bin. The innermost point in each temperature profile corresponds to the emission centered on the central elliptical galaxy. The profiles are given in Figure 3. Temperature profiles have previously been published for all three groups (NGC533 and NGC 2563: Trinchieri et al. 1997, HCG 62: Ponman & Bertram 1993, Pildis et al. 1995) and our results are consistent with these earlier studies. For the NGC 533 group, our three temperature measurements suggest an



isothermal distribution out to the radius of  $300 \text{ h}^{-1} \text{ kpc}$ . Trinchieri et al. (1997) bin the data into smaller annuli and find some indication that the gas temperature may rise slightly beyond the central point, although the uncertainties in their derived temperatures are large given the smaller number of counts in each bin. In the NGC 2563 group, the profile is consistent with an isothermal distribution beyond about  $2'$  ( $\sim 30 \text{ h}^{-1} \text{ kpc}$ ). However, the gas in the central region is cooler than the rest of the group by nearly 20%. A similar effect is seen in HCG 62, where the temperature of the gas rises from the center out to a radius of  $\sim 7'$  ( $\sim 90 \text{ h}^{-1} \text{ kpc}$ ) and then drops at large radii. Although we do not have enough counts to produce temperature profiles for the other groups, in at least one other case (NGC 741), the central component is significantly cooler than the extended gas (see Table 3). The lower temperature of the gas in the inner regions of these groups further supports the existence of a distinct component possibly associated with the central galaxy. The thermally cooler X-ray gas near the centers of these groups is consistent with the central galaxy being dynamically cooler (i.e., the velocity dispersion is lowest near the center of the group; see §3.3 of Paper I).

The luminosity of the X-ray emitting gas in each group has been estimated from the Raymond-Smith spectral model with the best fit abundance and the absorbing column fixed at the Galactic value. The X-ray luminosities depend on several assumptions. First, some authors have adopted a *mixed emission* scenario for groups (e.g., Mahdavi et al. 1997), where it is assumed that most of the group gas is associated with the potentials of individual galaxies. In these cases, the authors have included the contribution from the galaxies in the total X-ray emission. Other authors have excluded the emission from individual galaxies, preferring instead to measure the luminosity of the extended, diffuse gas only (e.g., Ponman et al. 1996). For all of the X-ray detected groups in our sample except HCG 90, the diffuse gas plus the central galaxy emission dominates the observed flux. Typically, these components account for 60–80% of the raw counts after background subtraction (the flux of the extended component is typically 2–10 times that of the central component). The remaining X-ray emission is associated with ‘point sources’. As described in §2, more than 90% of these ‘point sources’ appear to be unrelated to the group as a whole or even to the individual group galaxies. In fact, for three of the X-ray detected groups, the only X-ray emitting member is the BGG. Given that the majority of the ‘point source’ flux is completely unrelated to the global group potential or to the group galaxies, we exclude it from the calculated luminosities. However, since a fraction of the diffuse emission is lost when point sources are masked out, we have corrected the extended component luminosities for this “missing” flux by replacing the masked regions with interpolated values. This correction typically raises the diffuse luminosities by  $\sim 20\%$ .

We have also assumed the best-fit metallicities in calculating the luminosities.

Unfortunately, the X-ray luminosity is a strong function of the assumed metallicity and if our metallicities are lower by a factor of a few, the luminosities may be significantly overestimated (compare best-fit to 0.5 solar models in Table 3). The luminosities for the extended component, the central component and the combination of the extended + central components are given in Table 3. We have estimated errors in the luminosity by varying the temperature and metallicity parameters over their 90% confidence range (see Table 3). For the groups where X-ray luminosities have been published in the literature (e.g., Ponman et al. 1996; Trinchieri et al. 1997), there is good agreement between our derived luminosities and the values found by previous authors.

For the three groups where no diffuse emission is seen, we derive upper limits on the X-ray luminosities using a method similar to that described in Mulchaey et al. (1996a). We first measure the net counts in a region  $300 \text{ h}^{-1} \text{ kpc}$  in radius centered on each group. The counts are then converted to flux assuming a Raymond-Smith plasma model with temperature 1 keV and abundance 0.3 solar. All point sources in the field have been masked out as described above. Thus, the quoted luminosities correspond to upper limits for the *diffuse* X-ray emission in these groups. The diffuse emission  $\sim 14'$  north of the NGC 7582 group has been included in the calculation of the luminosity for this system. However, because this emission is almost certainly associated with the background cluster Abell S1111, the true group luminosity is probably much lower.

## 5. Discussion

The X-ray analysis presented in the last two sections argues strongly for the presence of two X-ray components in the X-ray detected groups: one restricted to the inner few tens of kiloparsecs of the group and one on the hundreds of kiloparsec scale. The existence of these two components is supported by the surface brightness profiles of the X-ray emission and by differences in the temperature of the gas between the inner and outer regions of the groups. In this section, we consider the nature of these components further.

As suggested earlier, the central component may originate in the interstellar medium of the BGG. The idea is supported by several observations. First, the location of the central component is always consistent with the optical position of the BGG (within  $\sim 5\text{--}10 \text{ h}^{-1} \text{ kpc}$ , one PSPC resolution element at the distances of these groups). The X-ray properties of the central component are also consistent with those expected for a luminous elliptical galaxy. For example, the core radius of the central component is in the range  $\sim 4$  to  $20 \text{ h}^{-1} \text{ kpc}$ , comparable to what has been found in previous studies of ellipticals (i.e.,

Forman, Jones & Tucker 1985; Thomas et al. 1986; Trinchieri, Fabbiano & Canizares 1986; Canizares, Fabbiano & Trinchieri 1987; Buote & Canizares 1994). The X-ray luminosity of the central component ( $\sim 10^{41-42} \text{ h}^{-2} \text{ erg s}^{-1}$ ) is consistent with the X-ray luminosity of other ellipticals of similar blue optical luminosity (e.g., Fabbiano, Kim & Trinchieri 1992; Eskridge et al. 1995). Finally, the temperature of the central component ( $\sim 0.7\text{--}0.9 \text{ keV}$ ) is in the range of temperatures found for elliptical galaxies with stellar velocity dispersions ( $\sim 200\text{--}300 \text{ km s}^{-1}$ ) similar to the BGG (e.g., Matsumoto et al. 1997). In summary, the location, extent, luminosity and temperature of the central component suggest that it is most likely associated with the BGG.

An alternative explanation for the central component is that it is the result of a large-scale cooling flow. Some of the X-ray signatures of cooling flows in clusters include sharply peaked surface brightness profiles, drops in the gas temperature near the center of the cluster and excess X-ray absorption (cf. Fabian 1994). In addition, many of the central galaxies in cooling flow clusters have unusual optical properties, such as strong, low-ionization emission-lines and diffuse blue light (e.g., Heckman et al. 1989; Crawford & Fabian 1992). The X-ray detected groups also display some of these signatures. In particular, the sharp upturn in the surface brightness profiles indicates that the gas density is rising steeply towards the center of groups, as expected in a cooling flow model. In contrast to expectations, however, the gas temperature near the center of some groups is comparable to the outer gas temperature (e.g., NGC 533). We have also searched for optical emission-lines in the BGGs using our fiber spectroscopy data, but no line emission is found.

While these observations do not necessarily rule out the cooling flow model, we believe the X-ray and optical data may be more naturally explained if the central component originates internally in the interstellar medium of the BGG. As described above, the X-ray properties of the central component are all consistent with those expected for elliptical galaxies. Furthermore, the cooler temperature of the central component in some groups is expected because the BGG tends to be dynamically cooler than the group as a whole (i.e., the velocity dispersion profile of the group also drops at the center; see §3.3 of Paper I). Future X-ray observations should help distinguish between an external (i.e., cooling flow) and internal (i.e., BGG interstellar medium) origin for the central component. Gas metallicity measurements, in particular, should provide insight into this problem.

The extended X-ray component can be traced to at least a radius of  $100\text{--}300 \text{ h}^{-1} \text{ kpc}$  in the X-ray detected groups. The large extent of this component suggests that it may be associated with the global group potential, much as the hot, diffuse gas in rich clusters is associated with the deep cluster potential well. We address this issue further by comparing our group sample with the large cluster sample in Mushotzky & Scharf (1997), which

includes clusters at low and intermediate redshift with well-determined X-ray temperatures and luminosities.

Because the collision time-scale for gas in groups and clusters is short compared to the gas cooling time, the temperature of the extended hot gas provides a tracer of the global potential. The velocity dispersion of the system also provides a measure of the potential. Our calculated velocity dispersions do not suffer from the statistical uncertainties that have previously made this quantity unreliable for groups, because we have measured velocities for at least 20–50 members in the X-ray detected groups. We plot the X-ray temperature versus the optical velocity dispersion for the group and cluster samples in Figure 4. The best-fit parameters and errors have been determined using the parametric bootstrap technique described in Lubin & Bahcall (1993). For the group sample, the best fit is:

$$\text{Log } \sigma_r = (2.56 \pm 0.06) + (0.45 \pm 0.19) \log T.$$

The fit to the entire sample of groups and clusters gives:

$$\text{Log } \sigma_r = (2.59 \pm 0.04) + (0.51 \pm 0.05) \log T$$

which is in good agreement with both the relationship we find for groups and the relationship found by others for rich clusters (e.g., Edge & Stewart 1991; Lubin & Bahcall 1993; Mushotzky & Scharf 1997).

As noted earlier, it is traditional to use the  $\beta$  parameter in clusters to infer the ratio of the average energy per unit mass in the galaxies to the average energy per unit mass in the gas. For a simple model where both the galaxies and the gas are isothermal and trace the same potential,  $\beta = 1$ . The best-fit value of  $\beta$  derived from our fit to the  $\sigma$ -T relationship for the group and cluster sample is  $\beta = 0.99 \pm 0.08$ , consistent with the isothermal model. The  $\beta$  determined for the group sample alone is also consistent with this value ( $\beta = 1.02 \pm 0.16$ ) and with the  $\beta$  value found from most of the surface brightness profiles (§3). This result conflicts with some earlier claims that most groups have  $\beta < 1$  (e.g., Ponman et al. 1996). We suspect these differences result from the ill-defined velocity dispersions used in previous studies. While a velocity dispersion determined from only three or four velocity measurements can either underestimate or overestimate the true group dispersion, a dispersion grossly in error is more likely to be underestimated (see Paper I). This bias could explain the trend Ponman et al. (1996) find for low values of  $\beta$ . The observation that the typical  $\beta$  value for groups is  $\sim 1$  implies that the cores of the X-ray detected groups are (on average) virialized. This conclusion is also supported by the optical kinematics of these groups (see Paper I).

The X-ray luminosity provides a measure of the total mass in hot gas. For rich clusters, there is a correlation between this quantity and the total mass of the system (as measured

by  $T$  or  $\sigma_r$ : Edge & Stewart 1991, David et al. 1993, Mushotzky & Scharf 1997). In Figure 5, we plot the X-ray luminosities of the hot gas versus the gas temperature. Although there is considerable scatter in the group sample alone, a similar scatter is found for the clusters. When the groups and clusters are considered together, a correlation is found. The fit to the entire sample gives:

$$\text{Log } L_X = (42.44 \pm 0.11) + \log h^{-2} + (2.79 \pm 0.14) \log T.$$

Ponman et al. (1996) find a significant steepening in the  $L_X$ - $T$  relationship for groups and suggest this may be evidence for the importance of galactic winds in low-mass systems. While we have too few points to determine a relationship for the group sample alone, we find no evidence for a steeper relationship at low ( $< 1$  keV) temperatures. Our groups are consistent with the observed cluster relation.

There is also a trend between X-ray luminosity and velocity dispersion for the group + cluster sample (Figure 6 and Table 4), although once again, the scatter is considerable:

$$\text{Log } L_X = (31.61 \pm 1.09) + \log h^{-2} + (4.29 \pm 0.37) \log \sigma_r.$$

We have not included the three non-X-ray detected groups in our derivation of the  $L_X$ - $\sigma_r$  relationship. We note, however, that the upper limits on the X-ray luminosities of the three non-detected groups are consistent with the luminosities expected given their low velocity dispersions (e.g., Mulchaey et al. 1996b; Ponman et al. 1996).

Two recent studies have suggested significant flattening of the  $L_X$ - $\sigma_r$  relationship for groups (Dell’Antonio et al. 1994; Mahdavi et al. 1997). The dashed line in Figure 6 gives the best-fit relationship Mahdavi et al. (1997) find for their sample of nine groups observed in the ROSAT all-sky survey. While most of our groups scatter around the midpoint of the Mahdavi et al. (1997) relationship, the much steeper extrapolation of the cluster relationship also provides an adequate description of the groups in our sample (Figure 6). Ponman et al. (1996) also find that a sample of Hickson Compact Groups are consistent with the cluster extrapolation. Mahdavi et al. (1997) suggest that the differences between their derived slope and that of Ponman et al. (1996) can be understood by two effects. First, the velocity dispersions used by Ponman et al. (1996) were based on an average of four galaxies and thus might not provide a good estimate of the group potential. Second, Ponman et al. (1996) have removed X-ray emission from individual galaxies, which according to the Dell’Antonio et al. (1994) model may be the dominant contribution to the total group X-ray emission.

Our sample should not suffer from the effects suggested by Mahdavi et al. (1997). In fact, the quality of both our optical and X-ray data is much higher than that used in most previous studies. However, like Ponman et al. (1996), we derive a  $L_X$ - $\sigma_r$  relationship

for groups that is consistent with what has been found for clusters. The difference between our result and that of Mahdavi et al. (1997) can probably be explained by the different techniques used to measure the X-ray luminosity. By excluding emission from individual galaxies, we are studying the X-ray emission associated with the global group potential. In contrast, Mahdavi et al. (1997) are studying the combined emission from the individual galaxies and the intragroup medium. Given the different quantities being compared, differences in the derived  $L_X$ - $\sigma_r$  relation would be expected. Furthermore, as groups tend not to span a large range in velocity dispersion or X-ray luminosity, it is difficult to determine a reliable  $L_X$ - $\sigma_r$  relationship for these systems alone from the limited number of groups with well-determined velocity dispersions and X-ray luminosities. A firm determination of the  $L_X$ - $\sigma_r$  relationship for groups will probably have to wait until many more groups have reliable X-ray and optical measurements. However, it does appear that when only the intragroup medium component is considered in the measurement of X-ray luminosity (as in the present paper), X-ray detected groups are consistent with the extrapolation of the cluster  $L_X$ - $\sigma_r$  relationship.

The fact that the extended X-ray component in groups follows the same  $L_X$ - $T$ - $\sigma_r$  relationships found for rich clusters of galaxies argues that these X-ray groups are low-mass extensions of the cluster phenomenon. Given this, the extended component can properly be thought of as the intragroup medium, in analogy to the intracluster medium in clusters. The nature of the non-X-ray detected groups is less clear. Based on the low velocity dispersions of these groups, we would not expect to detect diffuse emission in the ROSAT observations. Thus, the present X-ray observations do not allow us to determine whether the non-X-ray-detected groups are bound systems or just chance superpositions of galaxies along the line-of-sight.

Further evidence of the physical similarities of the X-ray groups and rich clusters may be found by considering the BGG-group interface. There is some evidence that the BGG “knows about” the extended group potential: there is a clear tendency for the diffuse X-ray emission to roughly align with the optical light of the galaxy in most cases. To quantify this trend, we have fit the light distributions of the central galaxy and the intragroup medium with ellipses (using the task ‘ellipse’ in IRAF). The ability to determine a reliable position angle (PA) from an ellipse fit depends on several factors. First, the PA is not a meaningful quantity when the ellipticity of the X-ray emission is very small. This is often true in the inner few arcminutes of the group. Here we only consider a X-ray PA measurement reliable when the ellipticity is greater than 0.1. The ability to measure a PA is also a function of the signal-to-noise ratio. For most of the groups, this restricts accurate X-ray PA measurements to radii less than  $10'$  ( $\sim 100$ - $200 h^{-1}$  kpc). Keeping these limits in mind, we plot the determined PA’s of the X-ray emission as a function of radius in Figure

7 for the seven groups with sufficient data (meaningful X-ray PA's cannot be measured for the NGC 5846 group and HCG 90 because of low ellipticity and low signal-to-noise ratio, respectively). Figure 7 reveals that the radial variations in the X-ray PA's of most of the groups are small (i.e., less than  $\sim 20$  degrees). The X-ray isophotes are more complex in NGC 2563 and NGC 4325, possibly indicating the presence of isophotal twisting.

We have also determined the optical PA's of the central galaxies from CCD images in the B-band (see Table 5 and Figure 7). These measurements are typically made at much smaller radii than the X-ray measurements. As can be seen from Figure 7, the optical PA of the central galaxy and the PA of the diffuse X-ray emission often align to within the errors of the measurements. In five of the seven groups, the optical and X-ray PA's agree to better than 20 degrees. The probability of this occurring randomly if the parent sample is uniform is less than  $7 \times 10^{-3}$ . We conclude that there is a strong trend for the optical light of the BGG and the global X-ray emission to align. A similar phenomenon has been seen in rich clusters containing cD galaxies (e.g., Rhee, van Haarlem & Katgert 1992; Sarazin et al. 1995; Allen et al. 1995), implying that the physical mechanisms responsible for the formation of the BGG and cD galaxies may be similar. The alignment of the central galaxy isophotes with the global group potential (as probed by the X-ray emission) is consistent with the BGG forming via galaxy mergers early in the lifetime of the group. The low velocity dispersions of groups make them a likely site for such mergers. Mergers are most probable during the initial formation of the group because at this point the galaxies still retain large halos (Merritt 1985). The fact that the BGG is at rest in the center of the group potential (Paper I) also suggests that the core of the group has not experienced much dynamical evolution recently and that it is near or at equilibrium.

## 6. Conclusions

We have presented ROSAT PSPC observations of twelve groups with detailed galaxy membership (Paper I). Diffuse X-ray emission is found in nine groups. The most luminous galaxy in each of the X-ray detected groups is an elliptical, whose position is coincident with the peak of the X-ray emission in all but one case. Surface brightness profiles of the X-ray emission strongly suggest the presence of two components in these groups: one on scales of  $\sim 20\text{--}40 h^{-1}$  kpc and one on much larger scales (of at least  $\sim 100\text{--}300 h^{-1}$  kpc). The temperatures of the central and extended components are significantly different in some groups, consistent with the interpretation that the components are distinct. The extent, temperature ( $\sim 0.7\text{--}0.9$  keV) and luminosity ( $\sim 10^{41\text{--}42} h^{-2}$  erg s $^{-1}$ ) of the first component

is consistent with that observed in elliptical galaxies in other environments, suggesting that this component most likely originates in the interstellar medium of the central galaxy. Alternatively, the central component may be the result of a cooling flow.

The extended X-ray component follows the extrapolation of the relationships found among velocity dispersion, X-ray temperature and X-ray luminosity for rich clusters. This suggests X-ray detected poor groups can be thought of as scaled-down versions of clusters, with the extended X-ray component in groups representing the intragroup medium, in analogy to the intracluster medium in clusters. The best fit to the  $\sigma_r$ -T relationship for X-ray groups and clusters gives a mean  $\beta$  value of  $0.99 \pm 0.08$ , suggesting the galaxies and hot gas trace the same potential and that the energy per unit mass in the gas and galaxies is equal. The values of  $\beta$  derived independently from fits to the surface brightness profiles are consistent with  $\beta \sim 1$  in many groups. The lower values of  $\beta$  implied from other studies may be due to significant underestimates of the group velocity dispersion and to contamination of the surface brightness profiles by the central galaxy X-ray emission.

While the ROSAT data suggest the presence of two independent X-ray components in these groups, it is clear that the formation and/or evolution of the central galaxy is somehow linked to the extended group potential. In particular, there is a strong trend for the optical isophotes of the central galaxy to align with the X-ray emission isophotes on large scales. This result might be expected if the central galaxy formed via galaxy-galaxy mergers early in the lifetime of the group and has not been recently disturbed. The fact that the central galaxy is at rest in the center of the group's potential (Paper I) is consistent with this scenario. A similar phenomenon has been observed in some clusters (e.g., Rhee, van Haarlem & Katgert 1992; Sarazin et al. 1995; Allen et al. 1995), offering further evidence of the similarities between X-ray luminous, poor groups and rich clusters.

The results of this paper demonstrate the insight that can be gained by combining detailed group membership information with quality X-ray observations. Still, there are many outstanding questions that can be addressed with further work. Our sample contains few non-X-ray detected or low temperature groups. We are in the process of extending our spectroscopy program to include more of these systems. Significant improvements in the X-ray observations can also be expected. Many groups have been observed with ASCA, which should help determine the metallicity of the intragroup medium, providing further constraints on the origin of this component. Higher spatial resolution observations will also allow the central galaxy-group interface to be studied in much more detail.

The authors would like to thank Lori Lubin for her assistance with the parametric bootstrap technique, Richard Mushotzky and Caleb Scharf for providing data from their



cluster sample, Dennis Zaritsky for a careful reading of the manuscript and the referee for useful comments that improved this paper. The authors also acknowledge valuable discussions with Mike Bolte, David Burstein, Julianne Dalcanton, David Davis, Megan Donahue, Lars Hernquist, Tod Lauer, Lori Lubin, Bill Mathews, Richard Mushotzky, Julio Navarro, Ian Smail and Dennis Zaritsky. This research was made possible with the use of the HEASARC and NED databases. JSM acknowledges partial support for this program from NASA grants NAG 5-2831 and NAG 5-3529 and from a Carnegie postdoctoral fellowship. AIZ acknowledges support from the Carnegie and Dudley Observatories, the AAS, NSF grant AST-95-29259, and NASA grant HF-01087.01-96A.

## REFERENCES

- Allen, S. W., Fabian, A. C., Edge, A. C., Bohringer, H., White, D. A. 1995, MNRAS, 275, 741
- Bauer, F., & Bregman, J. N. 1996, ApJ, 457, 382
- Buote, D. A., & Canizares, C. R. 1994, ApJ, 427, 86
- Burns, J. O., Ledlow, M. J., Loken, C., Klypin, A., Voges, W., Bryan, G. L., Norman, M. L., & White, R. A 1996, ApJ, 467, L49.
- Canizares, C. R., Fabbiano, G., & Trinchieri, G. 1987, ApJ, 312, 503
- Crawford, C. S., & Fabian, A. C. 1992, MNRAS, 259, 265
- David, L. P., Slyz, A., Jones, C., Forman, W., Vrtilik, S. D., & Arnaud, K. A., 1993, ApJ, 412, 479
- David, L. P., Jones, C., Forman, W., & Daines, S. 1994, ApJ, 428, 544
- Davis, D. S., Mulchaey, J. S., Mushotzky, R. F., & Burstein, D. 1996, ApJ, 460, 601
- Dell'Antonio, I. P., Geller, M. J., & Fabricant, D. G. 1994, AJ, 107, 427
- Diaferio, A., Geller, M. J., & Ramella, M. 1995, AJ, 109, 2293
- Doe, S. M., Ledlow, M. L., Burns, J. O., & White, R. A. 1995, AJ, 110, 46
- Ebeling, H, Voges, W., & Böhringer, H. 1994, ApJ, 436, 44
- Edge, A. C., & Stewart, G. C. 1991, MNRAS, 252, 428
- Eskrige, P. B., Fabbiano, G., & Kim, D.-W. 1995, ApJS, 97, 141
- Fabbiano, G., Kim, D.-W., & Trinchieri, G. 1992, ApJS, 80, 531
- Fabian, A. C. 1994, ARAA, 32, 277

- Forman, W., Jones, C., & Tucker, W. 1985, ApJ, 293, 102
- Hasinger, G., Turner, T. J., George, I. M., & Boese, G. 1992, NASA/GSFL Office of Guest Investigator Programs, Calibration Memo CAL/ROS/92-001
- Heckman, T. M., Baum, S. A., van Breugel, W. J. M., & McCarthy, P. 1989, ApJ, 338, 48
- Henry, J. P. et al. 1995, ApJ, 449, 422
- Hernquist, L., Katz, N., & Weinberg, D. H. 1995, ApJ, 442, 57
- Ikebe, Y. et al. 1996, Nature, 379, 427
- Lubin, L. M., & Bahcall, N. A. 1993, ApJ, 415, L17
- Mahdavi, A., Bohringer, H., Geller, M. J., & Ramella, M. 1997, ApJ, in press
- Makishima, K. 1995, in *Dark Matter*, American Institute of Physics, New York, ed. S. Holt & C. L. Bennett, p. 172
- Matsumoto, H. et al. 1997, ApJ, in press
- Mewe, R., Gronenschild, E. H., & van den Oord, G. H. J. 1985, AA Supl., 62, 197
- Merritt, D. 1985, ApJ, 289, 18
- Mulchaey, J. S., Davis, D. S., Mushotzky, R. F., & Burstein, D. 1993, ApJ, 404, L9
- Mulchaey, J. S., Davis, D. S., Mushotzky, R. F., & Burstein, D. 1996a, ApJ, 456, 80
- Mulchaey, J. S., Mushotzky, R. F., Burstein, D., & Davis, D. S. 1996b, ApJ, 456, L5
- Mushotzky, R. F., & Scharf, C. A. 1997, ApJ, in press
- Pildis, R. A., Bregman, J. N., & Evrard, A. E. 1995, ApJ, 443, 514
- Ponman, T. J., & Bertram, D. 1993, Nature, 363, 51
- Ponman, T. J., Bourner, P. D. J., Ebeling, H., & Bohringer, H. 1996, MNRAS, 283, 690
- Ramella, M., Geller, M. J., & Huchra, J. P. 1989, ApJ, 344, 57
- Rhee, G., Van Haarlem, M., & Katgert, P. 1992, AJ, 103, 1721
- Sarazin, C. L., Burns, J. O., Roettiger, K., & Mcnamara, B. R. 1995, ApJ, 447, 559
- Snowden, S. L., Mccammon, D., Burrows, D. N., & Mendehall, J. A. 1994, ApJ, 424, 714
- Stark, A. A., Gammie, C. F., Wilson, R. W., Bally, J., Linke, R. A., Heiles, C., & Hurwitz, M. 1992, ApJS, 79, 77
- Thomas, P. A., Fabian, A. C., Arnaud, K. A., Forman, W., & Jones, C. 1986, MNRAS, 222, 655
- Trinchieri, G., Fabbiano, G., & Canizares, C. R. 1986, ApJ, 310, 637

Trinchieri, G., Fabbiano, G., & Kim, D.-W. 1997, AA , 318, 361

Zabludoff, A. I, & Mulchaey, J. S. 1997, ApJ, submitted (Paper I)

**Table 1: Group Sample**

| Group    | $N_H$ | ROSAT obs. number | PSPC exposure |
|----------|-------|-------------------|---------------|
| NGC 491  | 2.01  | RP800473          | 2,250         |
| NGC 533  | 3.00  | RP600541          | 11,779        |
| NGC 664  | 2.85  | RP200468          | 7,531         |
| NGC 741  | 3.45  | RP800507          | 8,021         |
| NGC 2563 | 3.92  | RP600542          | 21,155        |
| HCG 42   | 5.32  | WP800359          | 11,799        |
| NGC 4325 | 1.73  | RP800490          | 5,322         |
| HCG 62   | 3.54  | WP800098          | 17,646        |
| NGC 5129 | 1.90  | RP800489          | 5,568         |
| NGC 5846 | 3.96  | RP600257          | 6,979         |
| HCG 90   | 1.52  | WP800419          | 12,973        |
| NGC 7582 | 1.93  | RP700333          | 7028          |

**Table 2: King Model Fits**

| Group    | Component | $R_{\text{core}}$<br>(arcminute) | $\beta$                | $\chi^2_{\text{R}}$ |
|----------|-----------|----------------------------------|------------------------|---------------------|
| (1)      | (2)       | (3)                              | (4)                    | (5)                 |
| NGC 533  | Extended  | $8.15^{+4.26}_{-2.82}$           | $0.83^{+0.36}_{-0.19}$ | 0.98                |
|          | Central   | $0.26^{+0.15}_{-0.09}$           | $0.70^{+0.15}_{-0.11}$ | 1.03                |
| NGC 741  | Extended  | $14.08^{+1.88}_{-1.66}$          | $1.00^2$               | 0.93                |
|          | Central   | $0.41^{+0.20}_{-0.19}$           | $0.73^{+0.16}_{-0.15}$ | 0.98                |
| NGC 2563 | Extended  | $11.15^{+4.02}_{-2.79}$          | $0.86^{+0.23}_{-0.17}$ | 1.02                |
|          | Central   | $0.24^{+0.24}_{-0.22}$           | $0.63^{+0.15}_{-0.15}$ | 1.01                |
| HCG 42   | Extended  | $3.61^{+1.39}_{-1.22}$           | $0.68^{+0.12}_{-0.08}$ | 1.21                |
|          | Central   | $0.65^{+0.30}_{-0.35}$           | $1.06^{+0.45}_{-0.33}$ | 1.32                |
| NGC 4325 | Extended  | $5.63^{+1.00}_{-0.94}$           | $1.00^2$               | 1.12                |
|          | Central   | $0.95^{+0.11}_{-0.13}$           | $1.00^2$               | 1.70                |
| HCG 62   | Extended  | $9.00^{+4.94}_{-3.51}$           | $0.63^{+0.28}_{-0.15}$ | 0.92                |
|          | Central   | $0.56^{+0.16}_{-0.16}$           | $0.79^{+0.10}_{-0.09}$ | 1.14                |
| NGC 5129 | Extended  | $4.19^{+1.13}_{-1.22}$           | $0.89^{+0.18}_{-0.14}$ | 0.89                |
|          | Central   | $0.58^{+0.18}_{-0.13}$           | $1.14^{+0.22}_{-0.19}$ | 0.98                |
| NGC 5846 | Extended  | $13.93^{+2.66}_{-2.27}$          | $0.83^{+0.41}_{-0.28}$ | 1.03                |
|          | Central   | $1.18^{+0.17}_{-0.15}$           | $0.75^{+0.09}_{-0.06}$ | 1.40                |
| HCG 90   | Extended  | $3.75^{+1.81}_{-1.20}$           | $0.89^{+0.24}_{-0.19}$ | 1.45                |

(1) - Group name.

(2) - Component fit: Extended = king model fit to the outer profile (see text), Central= king model fit to the inner profile with the outer profile constrained with the best-fit ‘Extended’ model.

(3) - Best fit core radius measured in arcminutes.

(4) - Best fit  $\beta$  value.

(5) - Reduced chi-squared value for the fit. For the ‘Central’ fit, the reduced chi-squared value given is that for the two king model fit to the entire profile (see text).

<sup>1</sup> parameter unconstrained with current data.

<sup>2</sup> parameter fixed in the profile fits.

**Table 3**  
**Spectral Analysis**

| Group    | Component          | $R_{\text{extent}}$<br>arcminutes | Temperature<br>(keV)   | Raymond-Smith<br>Abundance<br>(solar) | $\chi^2_{\text{R}}$ | Temperature<br>(keV)   | Meka<br>Abundance<br>(solar) | $\chi^2_{\text{R}}$ | $\text{Log } L_{\text{bolometric}}$<br>$\text{h}^{-2} \text{ erg s}^{-1}$ | $\beta_{\text{spec}}$ |
|----------|--------------------|-----------------------------------|------------------------|---------------------------------------|---------------------|------------------------|------------------------------|---------------------|---|-----------------------|
| NGC 491  | Extended           | 18.5                              | -                      | -                                     | -                   | -                      | -                            | -                   | < 40.11   | -                     |
| NGC 533  | Extended + Central | 19.6                              | $0.97^{+0.04}_{-0.07}$ | $0.44^{+0.41}_{-0.19}$                | 1.20                | $0.95^{+0.08}_{-0.07}$ | $0.29^{+0.18}_{-0.10}$       | 1.30                | $42.08 \pm 0.08$  | 1.45                  |
|          | Extended           | 19.6                              | $1.00^{+0.07}_{-0.04}$ | $0.20^{+0.17}_{-0.07}$                | 1.01                | $0.99^{+0.11}_{-0.11}$ | $0.15^{+0.09}_{-0.07}$       | 1.06                | $41.91 \pm 0.04$  | 1.41                  |
|          | Extended           | 19.6                              | $1.04^{+0.06}_{-0.06}$ | 0.5                                   | 1.25                | -                      | -                            | -                   | $41.87 \pm 0.03$  | 1.36                  |
|          | Central            | 1.5                               | $0.94^{+0.06}_{-0.06}$ | $0.47^{+0.30}_{-0.16}$                | 1.09                | $0.91^{+0.07}_{-0.05}$ | $0.36^{+0.16}_{-0.10}$       | 1.24                | $41.63 \pm 0.15$  | -                     |
| NGC 664  | Extended           | 13.1                              | -                      | -                                     | -                   | -                      | -                            | -                   | < 40.00   | -                     |
| NGC 741  | Extended + Central | 19.2                              | $1.04^{+0.14}_{-0.15}$ | $0.14^{+0.20}_{-0.09}$                | 1.26                | $1.06^{+0.22}_{-0.18}$ | $0.10^{+0.13}_{-0.06}$       | 1.27                | $41.98 \pm 0.13$  | 1.18                  |
|          | Extended           | 19.2                              | $1.17^{+0.51}_{-0.17}$ | $0.21^{+0.60}_{-0.17}$                | 1.19                | $1.29^{+0.38}_{-0.30}$ | $0.16^{+0.56}_{-0.13}$       | 1.20                | $41.88 \pm 0.14$  | 1.05                  |
|          | Extended           | 19.2                              | $1.31^{+0.52}_{-0.22}$ | 0.5                                   | 1.18                | -                      | -                            | -                   | $41.88 \pm 0.05$  | 0.94                  |
|          | Central            | 1.5                               | $0.76^{+0.09}_{-0.09}$ | $0.17^{+0.21}_{-0.08}$                | 0.90                | $0.71^{+0.10}_{-0.08}$ | $0.19^{+0.21}_{-0.08}$       | 0.95                | $41.28 \pm 0.17$  | -                     |
| NGC 2563 | Extended + Central | 21.6                              | $1.08^{+0.05}_{-0.08}$ | $0.16^{+0.10}_{-0.07}$                | 1.09                | $1.11^{+0.12}_{-0.11}$ | $0.11^{+0.07}_{-0.04}$       | 1.09                | $41.97 \pm 0.06$  | 0.68                  |
|          | Extended           | 21.6                              | $1.10^{+0.11}_{-0.07}$ | $0.18^{+0.12}_{-0.08}$                | 1.13                | $1.16^{+0.15}_{-0.13}$ | $0.12^{+0.10}_{-0.05}$       | 1.12                | $41.93 \pm 0.05$  | 0.67                  |
|          | Extended           | 21.6                              | $1.20^{+0.12}_{-0.11}$ | 0.5                                   | 1.61                | -                      | -                            | -                   | $41.90 \pm 0.03$  | 0.62                  |
|          | Central            | 1.5                               | $0.88^{+0.13}_{-0.07}$ | $0.20^{+0.15}_{-0.08}$                | 1.14                | $0.87^{+0.15}_{-0.15}$ | $0.18^{+0.11}_{-0.07}$       | 1.26                | $40.95 \pm 0.08$  | -                     |
| HCG 42   | Extended + Central | 8.0                               | $0.86^{+0.12}_{-0.19}$ | $0.17^{+0.59}_{-0.14}$                | 1.57                | $0.80^{+0.20}_{-0.20}$ | $0.13^{+0.35}_{-0.10}$       | 1.50                | $42.08 \pm 0.20$  | 0.34                  |
|          | Extended           | 8.0                               | $0.86^{+0.13}_{-0.20}$ | $0.18^{+0.77}_{-0.13}$                | 1.58                | $0.80^{+0.20}_{-0.20}$ | $0.13^{+0.43}_{-0.09}$       | 1.51                | $41.96 \pm 0.41$  | 0.34                  |
|          | Extended           | 8.0                               | $0.90^{+0.12}_{-0.10}$ | 0.5                                   | 1.58                | -                      | -                            | -                   | $41.89 \pm 0.03$  | 0.33                  |
|          | Central            | 1.5                               | $0.70^{+0.07}_{-0.05}$ | $0.22^{+0.22}_{-0.09}$                | 1.16                | $0.67^{+0.05}_{-0.05}$ | $0.29^{+0.40}_{-0.11}$       | 1.24                | $41.04 \pm 0.19$  | -                     |
| NGC 4325 | Extended + Central | 14.3                              | $0.80^{+0.04}_{-0.04}$ | $0.21^{+0.10}_{-0.07}$                | 0.60                | $0.75^{+0.05}_{-0.05}$ | $0.20^{+0.09}_{-0.05}$       | 0.63                | $42.65 \pm 0.10$  | 0.58                  |
|          | Extended           | 14.3                              | $0.78^{+0.10}_{-0.13}$ | $0.05^{+0.07}_{-0.02}$                | 0.45                | $0.74^{+0.13}_{-0.11}$ | $0.06^{+0.06}_{-0.04}$       | 0.46                | $42.40 \pm 0.12$  | 0.59                  |
|          | Extended           | 14.3                              | $0.86^{+0.18}_{-0.09}$ | 0.5                                   | 1.32                | -                      | -                            | -                   | $42.26 \pm 0.07$  | 0.54                  |
|          | Central            | 1.5                               | $0.81^{+0.06}_{-0.09}$ | $0.81^{+0.76}_{-0.31}$                | 1.28                | $0.74^{+0.06}_{-0.07}$ | $0.89^{+1.66}_{-0.31}$       | 1.30                | $42.30 \pm 0.25$  | -                     |
| HCG 62   | Extended + Central | 24.2                              | $0.87^{+0.04}_{-0.04}$ | $0.07^{+0.03}_{-0.03}$                | 1.18                | $0.86^{+0.06}_{-0.06}$ | $0.07^{+0.02}_{-0.03}$       | 1.20                | $42.34 \pm 0.05$  | 1.07                  |
|          | Extended           | 24.2                              | $0.89^{+0.11}_{-0.10}$ | $0.03^{+0.03}_{-0.03}$                | 1.05                | $0.88^{+0.12}_{-0.10}$ | $0.02^{+0.03}_{-0.02}$       | 1.04                | $42.23 \pm 0.05$  | 1.04                  |
|          | Extended           | 24.2                              | $1.10^1$               | 0.5                                   | 3.50                | -                      | -                            | -                   | (41.88)   | 0.85                  |
|          | Central            | 1.5                               | $0.86^{+0.03}_{-0.03}$ | $0.53^{+0.20}_{-0.13}$                | 0.84                | $0.82^{+0.03}_{-0.03}$ | $0.46^{+0.14}_{-0.10}$       | 1.24                | $41.65 \pm 0.14$  | -                     |

**Table 3, Cont.**  
**Spectral Analysis**

| Group                 | Component          | $R_{\text{extent}}$<br>arcminutes | Temperature<br>(keV)   | Raymond-Smith<br>Abundance<br>(solar) | $\chi^2_{\text{R}}$ | Temperature<br>(keV)   | Meka<br>Abundance<br>(solar) | $\chi^2_{\text{R}}$ | $\text{Log } L_{\text{bolometric}}$<br>$\text{h}^{-2} \text{ erg s}^{-1}$ | $\beta_{\text{spec}}$ |
|-----------------------|--------------------|-----------------------------------|------------------------|---------------------------------------|---------------------|------------------------|------------------------------|---------------------|---|-----------------------|
| NGC 5129 <sup>2</sup> | Extended           | 15.4                              | $0.62^{+0.13}_{-0.11}$ | $0.05^{+0.05}_{-0.03}$                | 0.74                | $0.60^{+0.12}_{-0.10}$ | $0.06^{+0.07}_{-0.04}$       | 0.76                | $42.15 \pm 0.16$  | 0.92                  |
|                       | Extended           | 15.4                              | $0.79^{+0.09}_{-0.14}$ | 0.5                                   | 1.37                | -                      | -                            | -                   | $42.11 \pm 0.07$  | 0.72                  |
| NGC 5846              | Extended + Central | 20.0                              | $0.68^{+0.04}_{-0.04}$ | $0.09^{+0.04}_{-0.03}$                | 1.35                | $0.65^{+0.03}_{-0.04}$ | $0.12^{+0.04}_{-0.04}$       | 1.54                | $41.58 \pm 0.07$  | 1.31                  |
|                       | Extended           | 20.0                              | $0.65^{+0.13}_{-0.09}$ | $0.02^{+0.04}_{-0.02}$                | 1.17                | $0.64^{+0.11}_{-0.09}$ | $0.02^{+0.03}_{-0.02}$       | 1.20                | $41.38 \pm 0.09$  | 1.37                  |
|                       | Extended           | 20.0                              | $0.96^1$               | 0.5                                   | 3.11                | -                      | -                            | -                   | (41.23)   | 0.93                  |
|                       | Central            | 3.0                               | $0.70^{+0.04}_{-0.04}$ | $0.29^{+0.12}_{-0.07}$                | 1.21                | $0.66^{+0.03}_{-0.04}$ | $0.44^{+0.24}_{-0.13}$       | 1.49                | $41.15 \pm 0.09$  | -                     |
| HCG 90                | Extended           | 14.0                              | $0.39^{+0.08}_{-0.07}$ | $0.02^{+0.02}_{-0.02}$                | 1.35                | $0.40^{+0.08}_{-0.07}$ | $0.02^{+0.03}_{-0.02}$       | 1.36                | $40.97 \pm 0.16$  | 0.89                  |
|                       | Extended           | 14.0                              | $0.25^1$               | 0.5                                   | 2.92                | -                      | -                            | -                   | (40.81)   | 0.98                  |
| NGC 7582              | Extended           | 43.0                              | -                      | -                                     | -                   | -                      | -                            | -                   | $< 40.47$   | -                     |

<sup>1</sup> Unconstrained.

<sup>2</sup> There are insufficient counts in the central galaxy to allow spectral fitting.

**Table 4**  
Correlation Statistics

| Quantity<br>(1)                          | Figure<br>(2) | <u>Groups</u> |              | <u>Clusters/Groups</u> |              |
|--|---------------|---------------|--------------|------------------------|--------------|
|  |               | $\tau$<br>(3) | Prob.<br>(4) | $\tau$<br>(5)          | Prob.<br>(6) |
| Temp. vs. $\sigma_r$<br>(extended comp.) | 4             | 1.0           | 0.94         | 1.34                   | > 0.99       |
| Temp. vs. $L_X$<br>(extended comp.)      | 5             | <0.01         | <0.01        | 1.36                   | > 0.99       |
| $\sigma_r$ vs. $L_X$<br>(extended comp.) | 6             | 0.11          | 0.17         | 1.35                   | > 0.99       |

Col. (1)–Quantities compared, Col. (2)–Corresponding figure number, Col. (3)–Kendall’s  $\tau$  parameter for X-ray detected groups only, Col. (4)–Probability of a correlation for X-ray detected groups only (1.00=100% probability of a correlation), Col. (5)–Kendall’s  $\tau$  parameter for sample of clusters of galaxies and X-ray detected groups, Col. (6)–Probability of a correlation for sample of clusters of galaxies and X-ray detected groups.

**Table 5**  
X-ray and BGG Position Angles

| Group    | $PA_{Xray}^1$<br>(degrees) | $PA_{BGG}^2$<br>(degrees) | $ PA_{Xray} - PA_{BGG} $<br>(degrees) |
|----------|----------------------------|---------------------------|---------------------------------------|
| NGC 533  | 61                         | 48                        | 13                                    |
| NGC 741  | 56                         | 88                        | 32                                    |
| NGC 2563 | -21                        | 84                        | 75                                    |
| HCG 42   | -29                        | -36                       | 7                                     |
| NGC 4325 | -17                        | 1                         | 18                                    |
| HCG 62   | 67                         | 71                        | 4                                     |
| NGC 5129 | -5                         | -13                       | 8                                     |

<sup>1</sup> Average position angle (measured from north towards east) of the X-ray emission over the radius interval plotted in Figure 7.

<sup>2</sup> Position angle (measured from north towards east) of the central group galaxy (BGG) at a mean isophotal B-band magnitude of 24.

### Figure Captions

Fig. 1a– Contour map of the X-ray emission in the NGC 491 group overlaid on the STScI digitized sky survey (field of view  $1^\circ \times 1^\circ$ ). No diffuse emission is detected. The contours correspond to  $2\sigma$  and  $3\sigma$  above the background. The data have been smoothed with a Gaussian of width  $30''$ .

Fig. 1b– Contour map of the diffuse emission in the NGC 533 group overlaid on the STScI digitized sky survey (field of view  $1^\circ \times 1^\circ$ ). The emission from the central galaxy has not been removed. The contours correspond to  $3\sigma$ ,  $6\sigma$ ,  $9\sigma$ ,  $18\sigma$ ,  $36\sigma$  and  $72\sigma$  above the background. The data have been smoothed with a Gaussian of width  $30''$ .

Fig. 1c– Contour map of the X-ray emission in the NGC 664 group overlaid on the STScI digitized sky survey (field of view  $1^\circ \times 1^\circ$ ). No diffuse emission is detected. The contours correspond to  $2\sigma$  and  $3\sigma$  above the background. The data have been smoothed with a Gaussian of width  $30''$ .

Fig. 1d– Contour map of the diffuse emission in the NGC 741 group overlaid on the STScI digitized sky survey (field of view  $1^\circ \times 1^\circ$ ). The emission from the central galaxy has not been removed. The contours correspond to  $3\sigma$ ,  $6\sigma$ ,  $9\sigma$ ,  $18\sigma$ ,  $36\sigma$  and  $72\sigma$  above the background. The data have been smoothed with a Gaussian of width  $30''$ .

Fig. 1e– Contour map of the diffuse emission in the NGC 2563 group overlaid on the STScI digitized sky survey (field of view  $1^\circ \times 1^\circ$ ). The emission from the central galaxy has not been removed. The contours correspond to  $3\sigma$ ,  $6\sigma$ ,  $9\sigma$ ,  $18\sigma$ ,  $36\sigma$  and  $72\sigma$  above the background. The data have been smoothed with a Gaussian of width  $30''$ .

Fig. 1f– Contour map of the diffuse emission in HCG 42 overlaid on the STScI digitized sky survey (field of view  $1^\circ \times 1^\circ$ ). The emission from the central galaxy has not been removed. The contours correspond to  $3\sigma$ ,  $6\sigma$ ,  $9\sigma$ ,  $12\sigma$ ,  $24\sigma$ ,  $60\sigma$  and  $120\sigma$  above the background. The data have been smoothed with a Gaussian of width  $30''$ .

Fig. 1g– Contour map of the diffuse emission in the NGC 4325 group overlaid on the STScI digitized sky survey (field of view  $1^\circ \times 1^\circ$ ). The emission from the central galaxy has not been removed. The contours correspond to  $3\sigma$ ,  $6\sigma$ ,  $9\sigma$ ,  $18\sigma$ ,  $36\sigma$  and  $72\sigma$  above the background. The data have been smoothed with a Gaussian of width  $30''$ .

Fig. 1h– Contour map of the diffuse emission in HCG 62 overlaid on the STScI digitized sky survey (field of view  $1^\circ \times 1^\circ$ ). The emission from the central galaxy has not been removed. The contours correspond to  $3\sigma$ ,  $6\sigma$ ,  $9\sigma$ ,  $15\sigma$ ,  $30\sigma$ ,  $60\sigma$  and  $120\sigma$  above the background. The data have been smoothed with a Gaussian of width  $30''$ .



Fig. 1i– Contour map of the diffuse emission in the NGC 5129 group overlaid on the STScI digitized sky survey (field of view  $1^\circ \times 1^\circ$ ). The emission from the central galaxy has not been removed. The contours correspond to  $3\sigma$ ,  $6\sigma$ ,  $9\sigma$  and  $18\sigma$  above the background. The data have been smoothed with a Gaussian of width  $30''$ .

Fig. 1j– Contour map of the diffuse emission in the NGC 5846 group overlaid on the STScI digitized sky survey (field of view  $1^\circ \times 1^\circ$ ). The emission from the central galaxy has not been removed. The contours correspond to  $3\sigma$ ,  $6\sigma$ ,  $9\sigma$ ,  $18\sigma$ ,  $36\sigma$ ,  $72\sigma$  and  $144\sigma$  above the background. The data have been smoothed with a Gaussian of width  $30''$ .

Fig. 1k– Contour map of the diffuse emission in HCG 90 overlaid on the STScI digitized sky survey (field of view  $1^\circ \times 1^\circ$ ). The contours correspond to  $2\sigma$ ,  $3\sigma$ ,  $4\sigma$  and  $5\sigma$  above the background. The data have been smoothed with a Gaussian of width  $30''$ .

Fig. 1l– Contour map of the X-ray emission in the NGC 7582 group overlaid on the STScI digitized sky survey (field of view  $1^\circ \times 1^\circ$ ). The X-ray emission  $\sim 14'$  north of the group center is coincident with the optical position of the background cluster Abell S1111 and presumably not related to the NGC 7582 group. The emission in the north-east corner is associated with the rich cluster Abell 3998. No diffuse emission from the NGC 758 group itself is detected. The contours correspond to  $3\sigma$ ,  $6\sigma$ ,  $12\sigma$ ,  $30\sigma$  and  $60\sigma$  above the background. The data have been smoothed with a Gaussian of width  $30''$ .

Fig. 2–Surface brightness profiles for the nine X-ray detected groups. The central galaxy emission has not been removed, except in the case of HCG 90. All other point sources in the field have been excluded. The dashed line shows the best-fit King model to the extended gas component, while the dotted line gives the best King model to the central emission. The solid line shows the overall two King model fit to the data. The ROSAT PSPC point spread function for a 1 keV source is plotted as the dotted-dashed line in the panel for NGC 533.

Fig. 3–Temperature profiles for NGC 533, NGC 2563 and HCG 62. The inner point in each profile corresponds to emission predominantly from the central component. Note the lower galaxy temperatures in the centers of NGC 2563 and HCG 62.

Fig. 4–Logarithm of the X-ray temperature vs. logarithm of optical velocity dispersion for groups (circles) and clusters (triangles). The cluster data are taken from Mushotzky & Scharf (1997). The X-ray temperature of the groups is for the extended component only. The straight line gives the best-fit to the entire dataset, which corresponds to  $\beta = 0.99 \pm 0.08$ .

Fig. 5–Logarithm of X-ray temperature vs. logarithm of X-ray luminosity. The symbols

have the same meaning as in Figure 4. For the groups, the luminosity plotted is for the extended component only. The total X-ray luminosities would typically be higher by  $\sim 20\%$  if the emission from the central galaxy was included. The solid line gives the best-fit to the data.

Fig. 6—Logarithm of velocity dispersion vs. logarithm of X-ray temperature for the X-ray detected groups (filled circles) and clusters (triangles). The non-X-ray detected groups are plotted using the upper limits on  $L_X$  (arrows). As in Figure 5, the group luminosity plotted is for the extended component only. The solid line gives the best-fit to the data (the groups with upper limits are not included in the fit). The dashed line is the best-fit that Mahdavi et al. (1997) find for their group sample (plotted over the velocity dispersion range in their Figure 4).

Fig. 7—Plots of the position angle (PA) of the X-ray emission versus radius as determined from ellipse fits to the isophotes of the ROSAT images. The PA is only determined over the radius range where the ellipticity is greater than 0.1 (points where the ellipticity is less than 0.1 are plotted as open squares). The dotted line gives the average PA of the X-ray emission over the plotted radius interval. The dashed line represents the optical PA of the BGG at a mean isophotal B-magnitude of 24 (see Table 5). Note the close alignment of the X-ray and optical PA's in many of the groups.

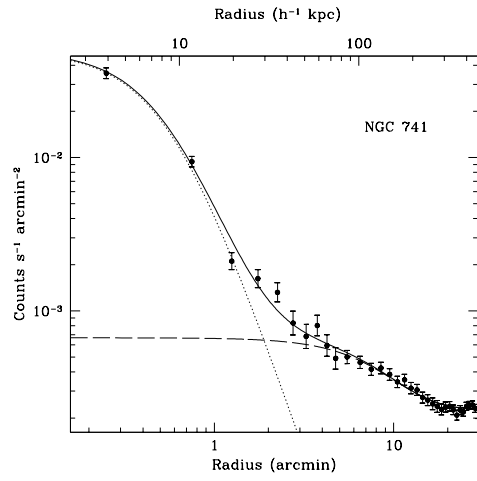
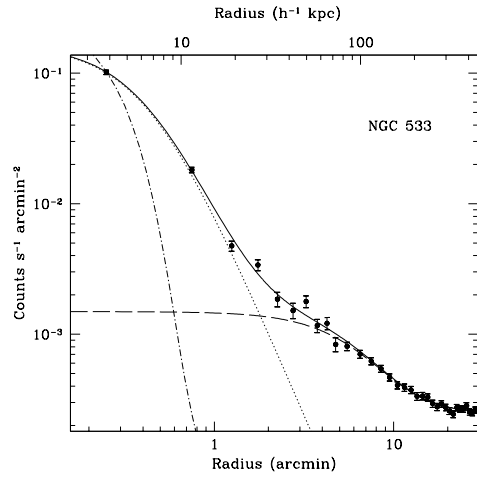


Figure 2

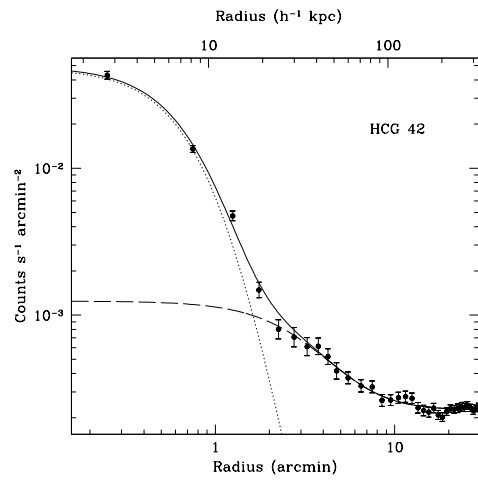
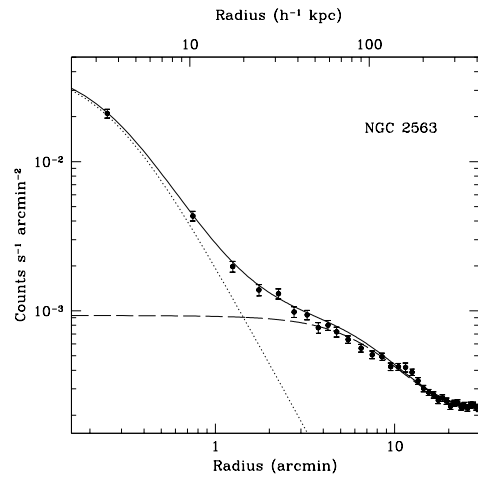


Figure 2

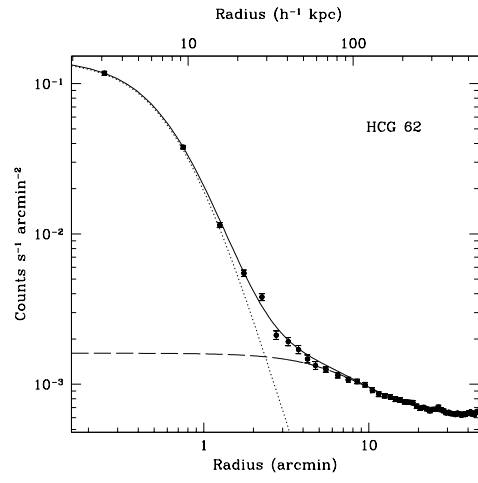
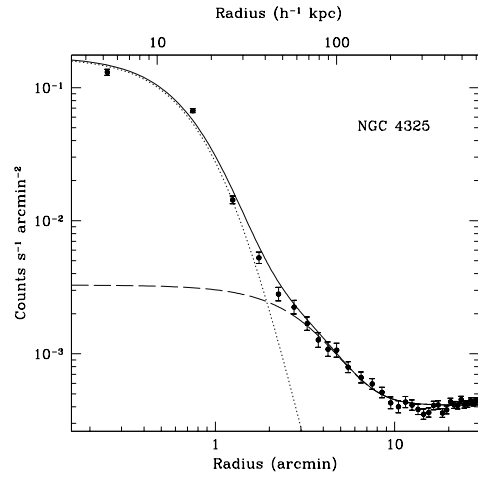


Figure 2

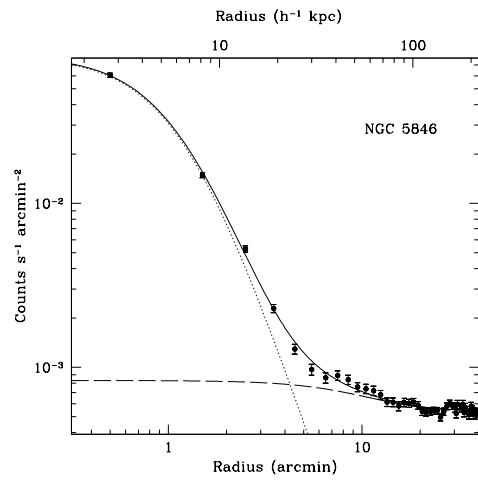
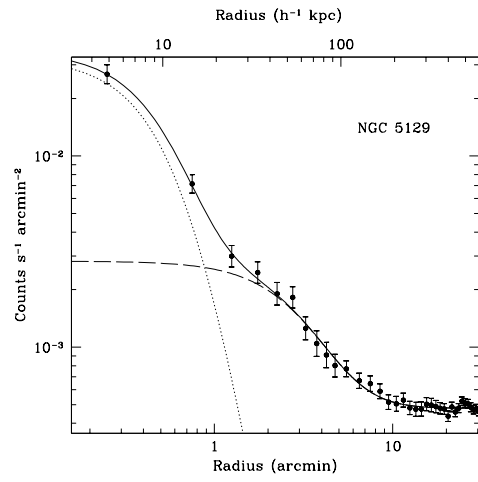


Figure 2

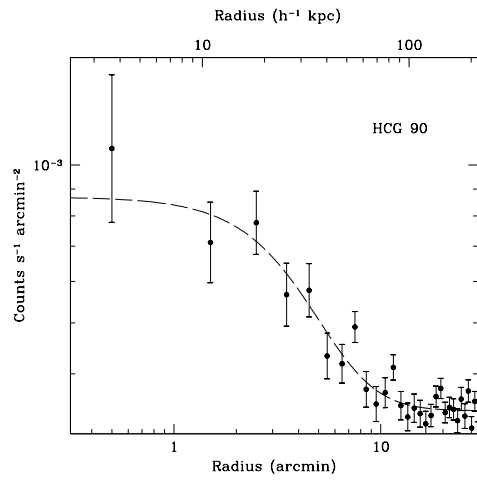


Figure 2

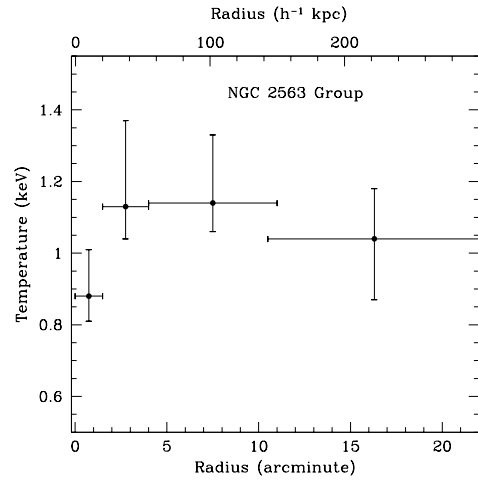
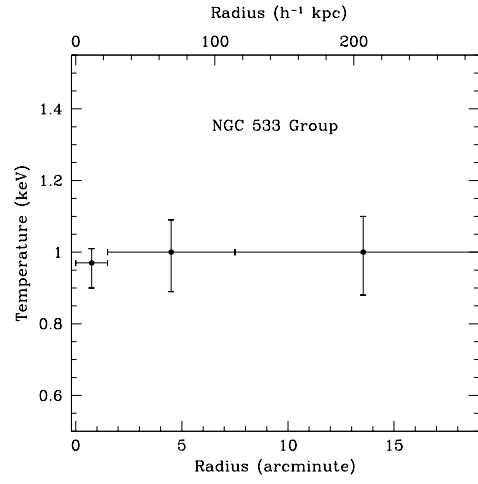


Figure 3



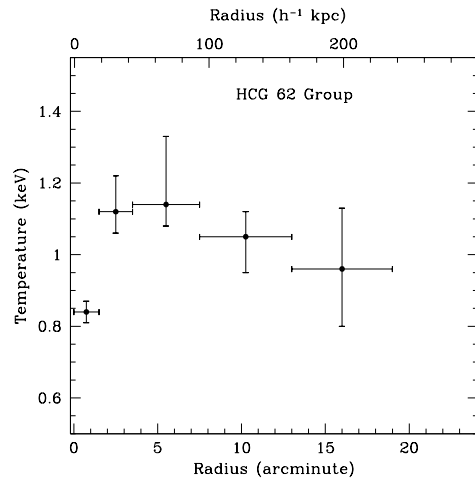


Figure 3

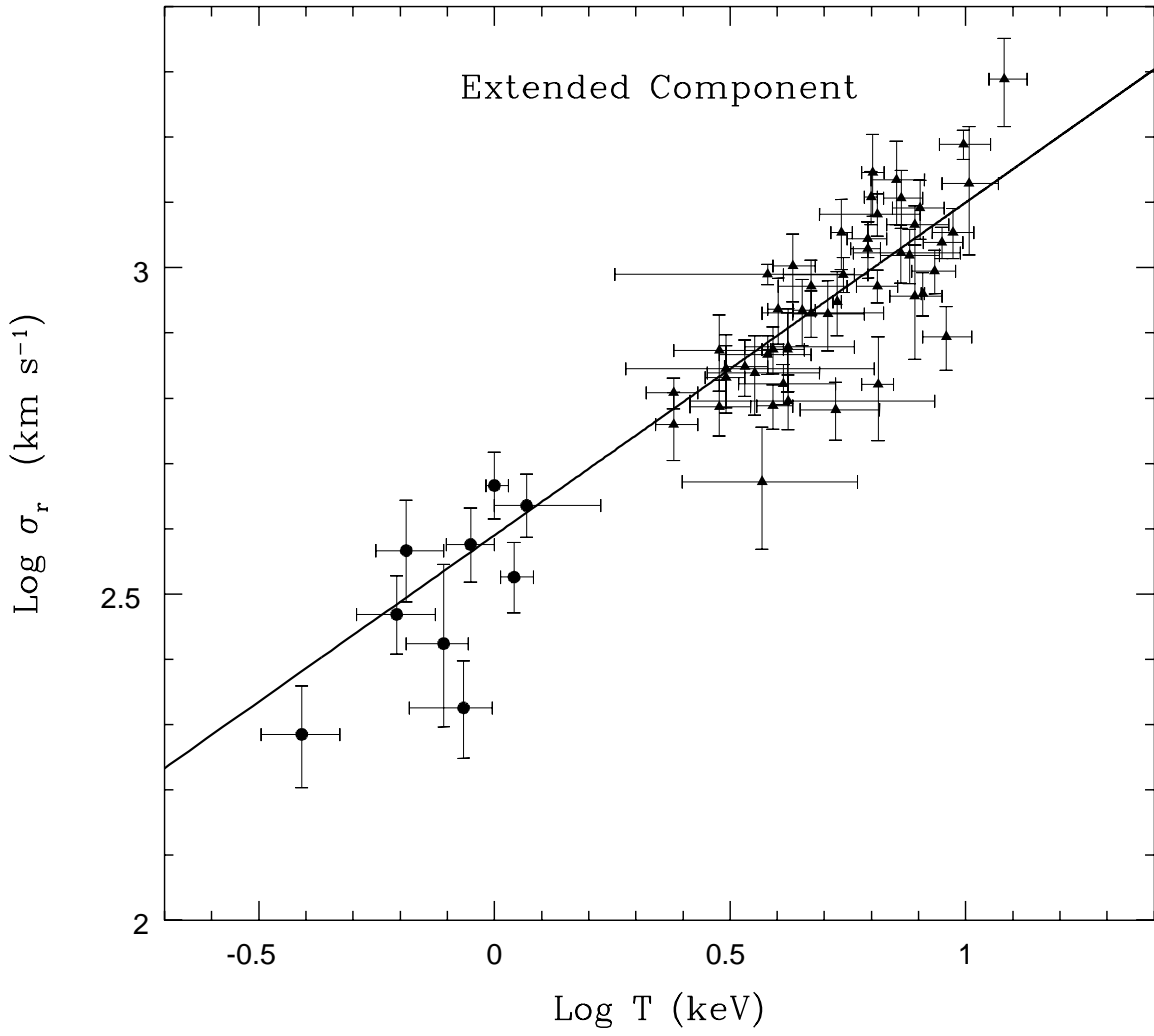


Figure 4

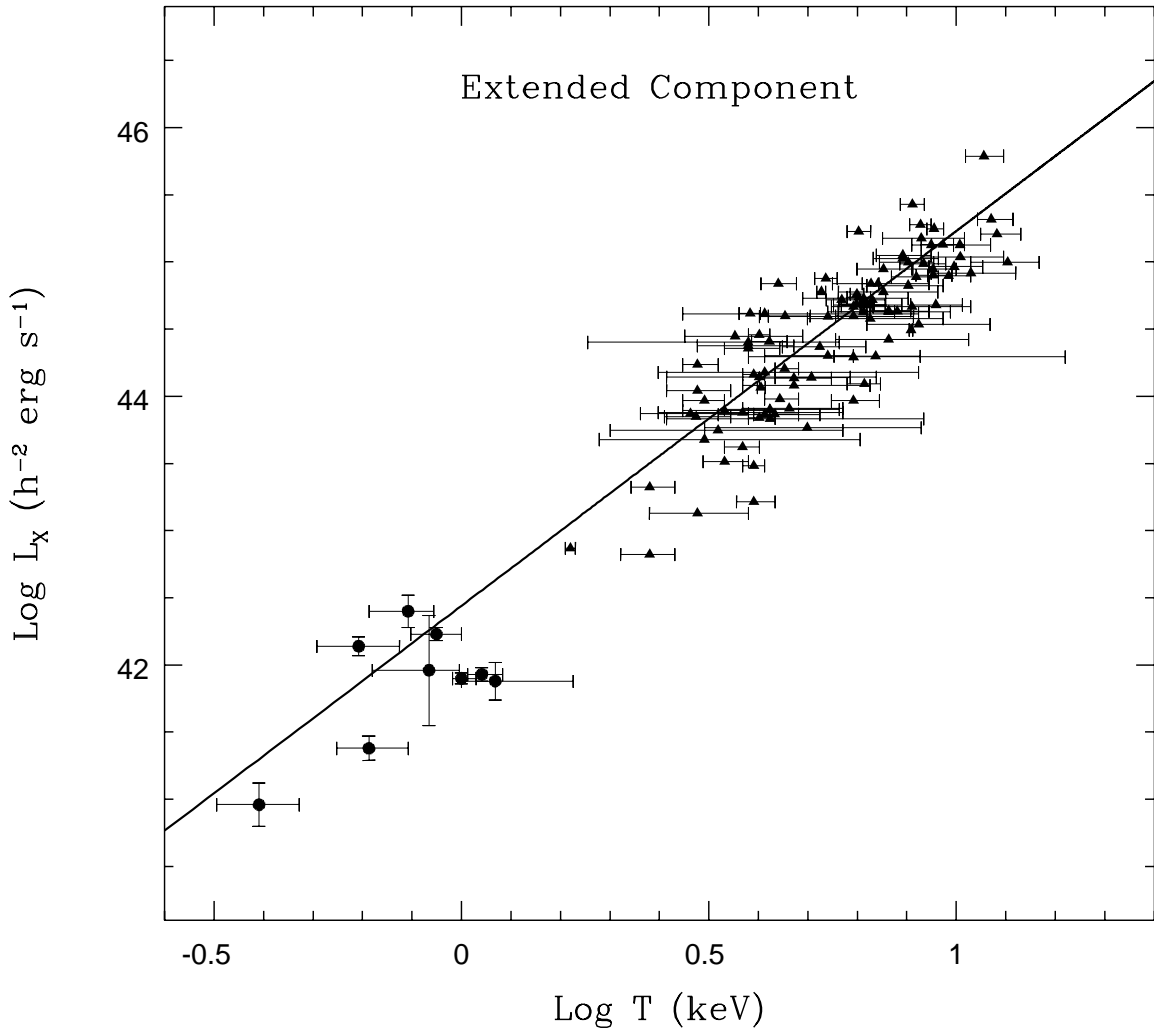


Figure 5

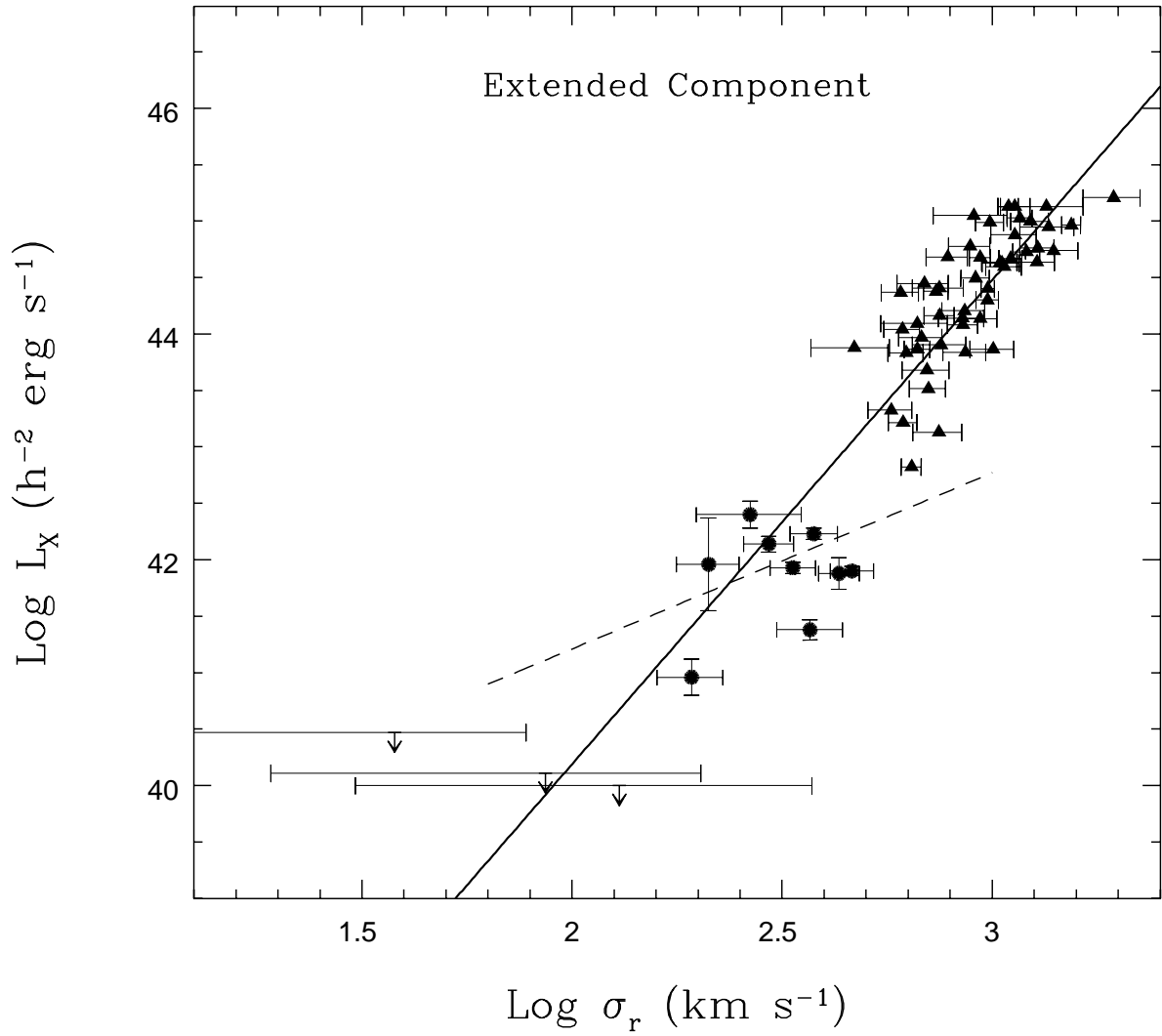


Figure 6

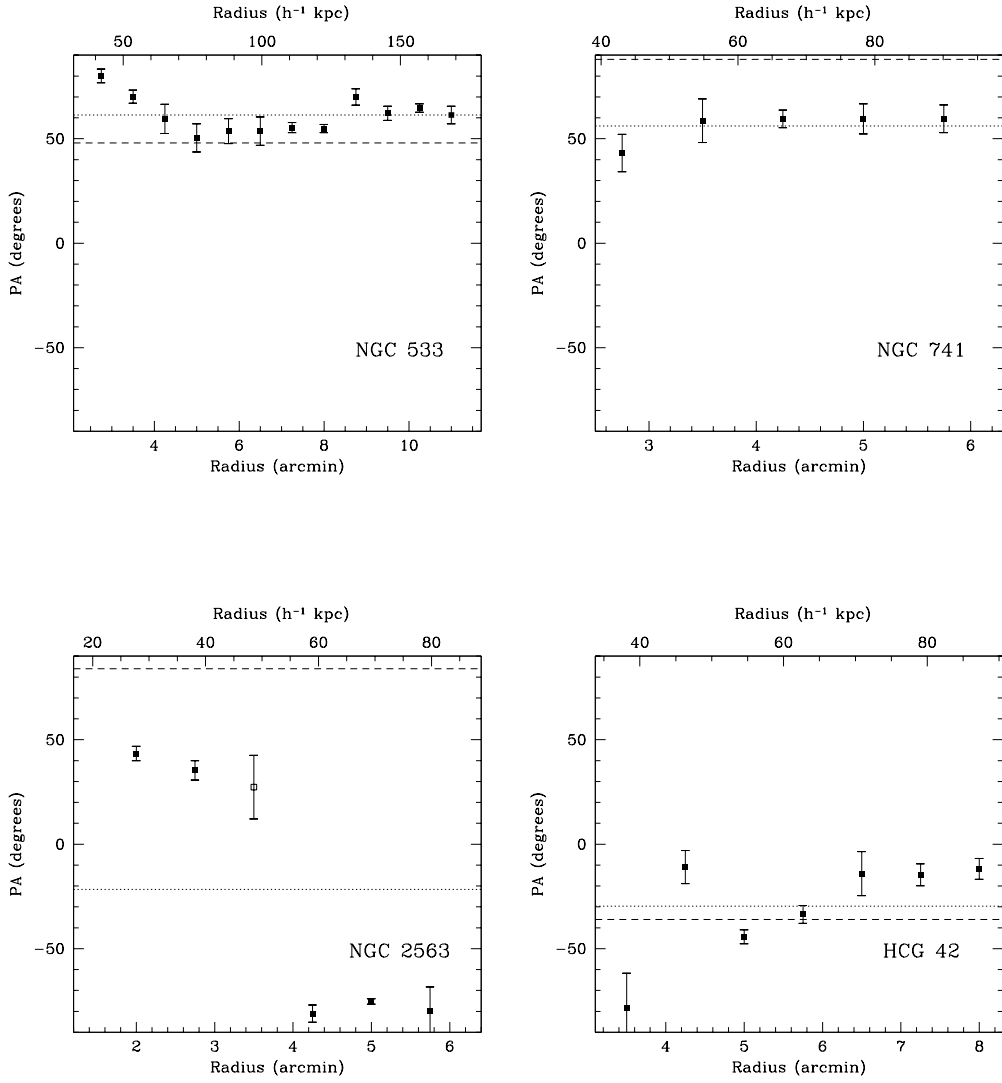


Figure 7

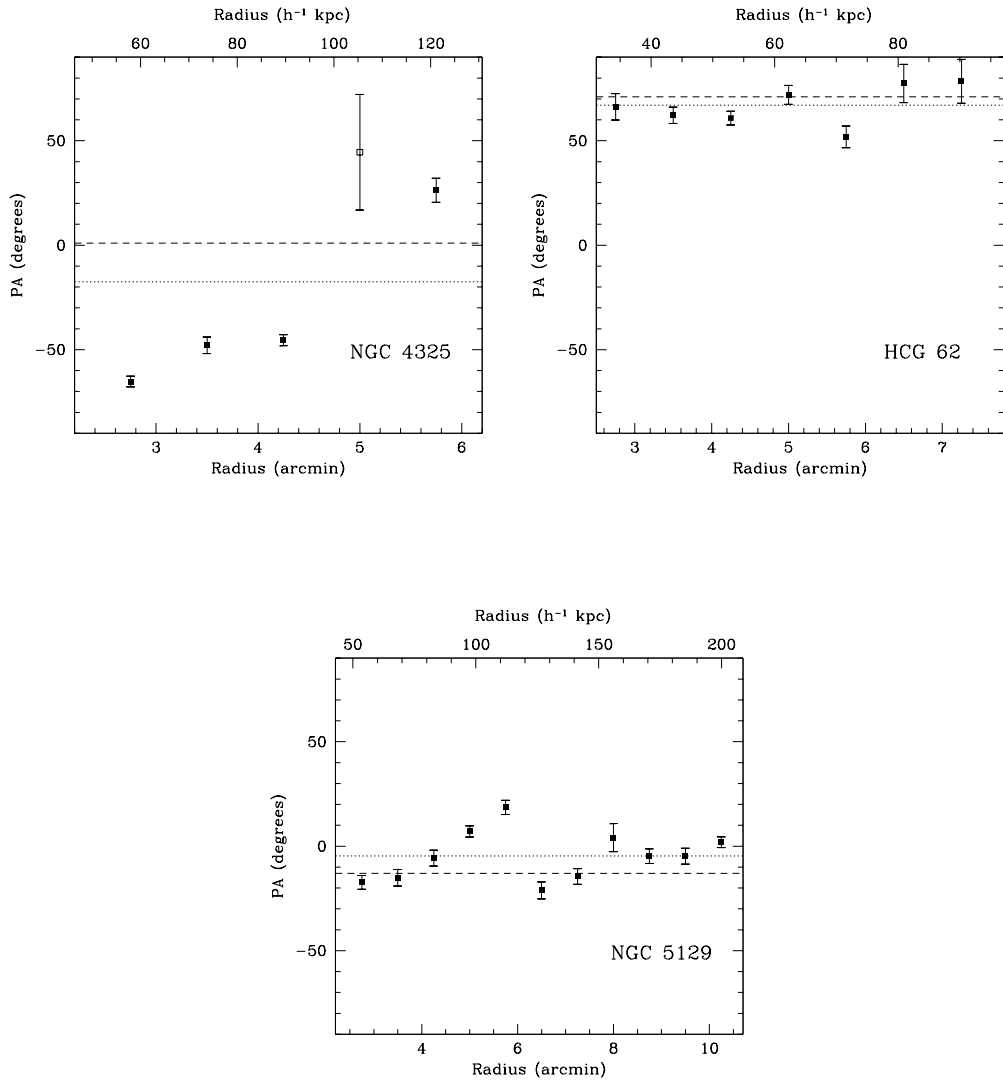


Figure 7

This figure "fig1a.gif" is available in "gif" format from:

<http://arxiv.org/ps/astro-ph/9708139v1>

This figure "fig1b.gif" is available in "gif" format from:

<http://arxiv.org/ps/astro-ph/9708139v1>



This figure "fig1c.gif" is available in "gif" format from:

<http://arxiv.org/ps/astro-ph/9708139v1>

This figure "fig1d.gif" is available in "gif" format from:

<http://arxiv.org/ps/astro-ph/9708139v1>

This figure "fig1e.gif" is available in "gif" format from:

<http://arxiv.org/ps/astro-ph/9708139v1>

This figure "fig1f.gif" is available in "gif" format from:

<http://arxiv.org/ps/astro-ph/9708139v1>

This figure "fig1g.gif" is available in "gif" format from:

<http://arxiv.org/ps/astro-ph/9708139v1>

This figure "fig1h.gif" is available in "gif" format from:

<http://arxiv.org/ps/astro-ph/9708139v1>

This figure "fig1i.gif" is available in "gif" format from:

<http://arxiv.org/ps/astro-ph/9708139v1>

This figure "fig1j.gif" is available in "gif" format from:

<http://arxiv.org/ps/astro-ph/9708139v1>



This figure "fig1k.gif" is available in "gif" format from:

<http://arxiv.org/ps/astro-ph/9708139v1>

This figure "fig11.gif" is available in "gif" format from:

<http://arxiv.org/ps/astro-ph/9708139v1>